2D graphene oxide: a versatile thermo-optic material

Junkai Hu, Jiayang Wu, Wenbo Liu, Di Jin, Houssein El Dirani, Sébastien Kerdiles, Corrado Sciancalepore, Pierre Demongodin, Christian Grillet, Christelle Monat, et al.

To cite this version:

Junkai Hu, Jiayang Wu, Wenbo Liu, Di Jin, Houssein El Dirani, et al.. 2D graphene oxide: a versatile thermo-optic material. Advanced Functional Materials, 2024, 2024, pp.2406799. 10.1002/adfm.202406799 . cea-04756420

HAL Id: cea-04756420
https://cea.hal.science/cea-04756420v1

Submitted on 28 Oct 2024

ADVANCED FUNCTIONAL MATERIALS
www.afm-journal.de

2D Graphene Oxide: A Versatile Thermo-Optic Material

Junkai Hu, Jiayang Wu, Wenbo Liu, Di Jin, Houssein El Dirani, Sébastien Kerdiles, Corrado Sciancalepore, Pierre Demongodin, Christian Grillet, Christelle Monat, Duan Huang,* Baohua Jia,* and David J. Moss**

Efficient heat management and control in optical devices, facilitated by advanced thermo-optic materials, are critical for many applications such as photovoltaics, thermal emitters, mode-locked lasers, and optical switches. Here, a range of thermo-optic properties of 2D graphene oxide (GO) films are investigated by precisely integrating them onto microring resonators (MRRs) with control over the film thicknesses and lengths. The refractive index, extinction coefficient, thermo-optic coefficient, and thermal conductivity for the GO films with different layer numbers and degrees of reduction, as well as reversible reduction and enhanced optical bistability induced by the photo-thermal effects, are comprehensively characterized. Experimental results show that the thermo-optic properties of 2D GO films vary widely with the degree of reduction. In addition, significant anisotropy is observed for the thermo-optic response, enabling efficient polarization-sensitive devices. The versatile thermo-optic response of 2D GO substantially expands the scope of functionalities and devices that can be engineered, making it promising for a diverse range of thermo-optic applications.

1. Introduction

As a fundamental phenomenon, heat transfer induced by temperature difference is closely related to people's daily lives.[1] The management and control of heat are important for tackling issues like global warming, energy shortages, and device overheating. In terms of optical applications, controlling heat via harnessing the material property changes induced by thermo-optic effects has underpinned the functionality and efficiency of many optical devices and systems such as photovoltaics,[2,3] thermal emitters,[4,5] mode-locked lasers,[6,7] optical switches,[8,9] logic gates,[10,11] power limiters,[12,13] optical memories,[14,15] and sensors.[16,17]

Over the past two decades, the rapid advances in material science have provided powerful tools to efficiently manipulate

---

J. Hu, J. Wu, W. Liu, D. Jin, D. J. Moss
Optical Sciences Centre
Swinburne University of Technology
Hawthorn, VIC 3122, Australia
E-mail: jiayangwu@swin.edu.au; dmoss@swin.edu.au

J. Hu, D. Jin
School of Automation
Central South University
Changsha 410083, China

J. Wu, C. Grillet, C. Monat, B. Jia, D. J. Moss
ARC Centre of Excellence in Optical Microcombs for Breakthrough Science (COMBS)
Melbourne, VIC 3000, Australia

The ORCID identification number(s) for the author(s) of this article can be found under https://doi.org/10.1002/adfm.202406799

[+]Present address: LIGENTEC SA, Corbeil-Essonnes 91100, France
[++]Present address: Soitec SA, Bernin 38190, France

DOI: 10.1002/adfm.202406799

W. Liu, B. Jia
School of Science
Centre for Atomaterials and Nanomanufacturing
Australian Research Council (ARC) Industrial Transformation Training Centre in Surface Engineering for Advanced Materials (SEAM)
RMIT University
Melbourne, VIC 3000, Australia
E-mail: baohua.jia@rmit.edu.au

H. E. Dirani[+], S. Kerdiles, C. Sciancalepore[++]
Université Grenoble-Alpes
CEA-LETI
Minatec
Optics and Photonics Division
Grenoble 38054, France

P. Demongodin, C. Grillet, C. Monat
Institut des nanotechnologies de Lyon
UMR CNRS 5270
Ecole Centrale Lyon
Ecully F-69130, France

D. Huang
School of Electronic Information
Central South University
Changsha 410083, China
E-mail: duanhuang@csu.edu.cn

D. Huang
Hefei National Laboratory
Hefei 230088, China

heat transfer in optical devices.[18,19] This has been particularly facilitated by the emergence of many novel 2D materials with atomic thicknesses, such as graphene, transition metal dichalcogenides (TMDCs), and hexagonal boron nitride (hBN).[20–22] These 2D materials exhibit many remarkable thermo-optic properties, such as the ability to efficiently tune the refractive index and absorption via photo-thermal effects, high thermal conductivity, and anisotropic thermal-optic response. These have enabled a range of high-performance devices with new functionalities compared to those based on conventional bulk materials.[23,24]

As a common derivative of graphene, graphene oxide (GO) is a rising star in the 2D material family.[25–27] It exhibits many distinctive optical properties, such as a broadband response, high optical nonlinearity, and significant anisotropy.[28–30] There is also a high degree of flexibility in engineering GO's properties through reduction and doping processes,[17,31,32] offering a flexible platform for engineering a wide range of functionalized materials. Moreover, facile solution-based synthesis processes and transfer-free film coating with precise control of the layer number have been developed for 2D GO films,[33–35] with a high degree of compatibility with integrated device platforms.

In this paper, we comprehensively investigate a series of fascinating thermo-optic properties of 2D GO films by integrating them onto silicon nitride (SiN) microring resonators (MRRs) with precise control over the film thicknesses and lengths. We characterize the refractive index, extinction coefficient, thermo-optic coefficient, and thermal conductivity of 2D layered GO films for different layer numbers and degrees of reduction. Experimental results show that the thermo-optic properties of 2D GO films vary widely as the degree of reduction increases, including an increase of ≈0.2280 in the refractive index, a more than 36-fold increase in the extinction coefficient, a transition from a positive thermo-optic coefficient to a negative one, and over ≈60 times improvement in the thermal conductivity. In addition, the GO films show a markedly anisotropic response for light in transverse electric (TE) and transverse magnetic (TM) polarizations, including a difference of ≈0.14 for the refractive index, a ratio of ≈4 for the extinction coefficient, a ratio of ≈6 for the thermo-optic coefficient, and a ratio of ≈21 for the thermal conductivity. We also characterize reversible GO reduction and optical bistability in the hybrid MRRs induced by photo-thermal effects. Experimental findings reveal that reversible GO reduction can be initiated by light power within a specific range, and the hybrid MRRs exhibit significantly enhanced optical bistability compared to uncoated MRRs. These results offer interesting insights into the versatile thermo-optic properties of 2D layered GO films, which offer significant potential for a variety of thermo-optic applications.

2. Device Design and Fabrication

Figure 1a illustrates the atomic structures and bandgaps of GO, semi-reduced GO (srGO), and totally reduced GO (trGO). As a derivative of graphene, GO contains various oxygen functional groups (OFGs), such as hydroxyl, epoxide, carbonyl, and carboxylic groups, located either on the carbon basal plane or at the sheet edges.[25] Unlike graphene, which possesses a zero bandgap, the presence of the OFGs in GO results in a large optical bandgap ΔE typically ranging between ≈2.1 and ≈3.6 eV.[27,36] Due to its large optical bandgap, GO exhibits low linear optical absorption at infrared wavelengths, which is ≈2 orders of magnitude lower than that of graphene.[37] The reduction of GO leads to the dissociation of OFGs, along with the decrease of ΔE and the change of the material properties such as refractive index, optical absorption, and thermal conductivity.[26] Practically, the reduction of GO films can be realized by using various thermal reduction, chemical reduction, or photoreduction methods.[25] The bandgap and optical properties of trGO are similar to graphene, with slight differences arising from the defects within the carbon networks.[38]

Figure 1b shows a schematic of an integrated SiN MRR coated with a 2D GO film. Figure 1c shows a microscopic image of a fabricated device integrated with a film including 3 layers of GO, with the inset showing a scanning electron microscopy (SEM) image of the layered GO film. The SiN MRR was fabricated via CMOS-compatible and crack-free processes, as reported previously.[30,39] A 2.3-μm-thick silica layer was deposited on top of the fabricated SiN MRRs as an upper cladding. To facilitate the interaction between the GO film and the evanescent field of the SiN MRR, lithography and dry etching processes were employed to open a window in the silica cladding, extending down to the top surface of the SiN MRR. The coating of the 2D layered GO film was realized by using a solution-based method that allowed transfer-free and layer-by-layer film deposition.[33,40] During the coating process, 4 steps were repeated to assemble a multilayered film consisting of alternating GO monolayers and polymer layers with oppositely charged surfaces. As can be seen from Figure 1c, the coated GO film exhibits high transmittance and good morphology. The film also shows a high uniformity without any noticeable wrinkling or stretching. The thickness of the self-assembled GO film increases almost linearly with the number of GO layers, with an average thickness of ≈2 nm for each layer. Our GO coating method enables large-area film coating with precisely controlled film thickness, which was also used for on-chip integration of 2D GO films to realize other functional devices.[17,28,30,32,35]

Figure 1d shows the measured Raman spectra for the SiN chip before and after coating 1 layer of GO, which were measured using a ≈514-nm pump laser. The presence of the representative D (1345 cm^{-1}) and G (1590 cm^{-1}) peaks of GO in the Raman spectrum for the GO-coated chip confirms the successful integration of the GO film onto the chip.

In our fabricated SiN MRRs, the cross-section of the waveguides forming the MRRs (including both the ring and the bus waveguide) was ≈1.60 × 0.72 μm, as illustrated in Figure 1e. The inset shows a schematic of the layered GO film fabricated by self-assembly. Figure 1f shows the TE and TM mode profiles for the hybrid waveguide with 3 layers of GO in Figure 1e, which were simulated using commercial mode-solving software (COMSOL Multiphysics). The corresponding effective refractive indices at 1550 nm were $n_{eff,\,TE}$ = ≈1.784 and $n_{eff,\,TM}$ = ≈1.713. In our simulation, the refractive indices of GO and SiN at 1550 nm were $n_{\mathrm{GO}} = 1.972$ and $n_{\mathrm{SiN}} = 1.990$, respectively. These values were obtained from our experiments introduced in the following sections. Figure 1g shows GO mode overlap versus GO layer number for both TE and TM polarizations, which were

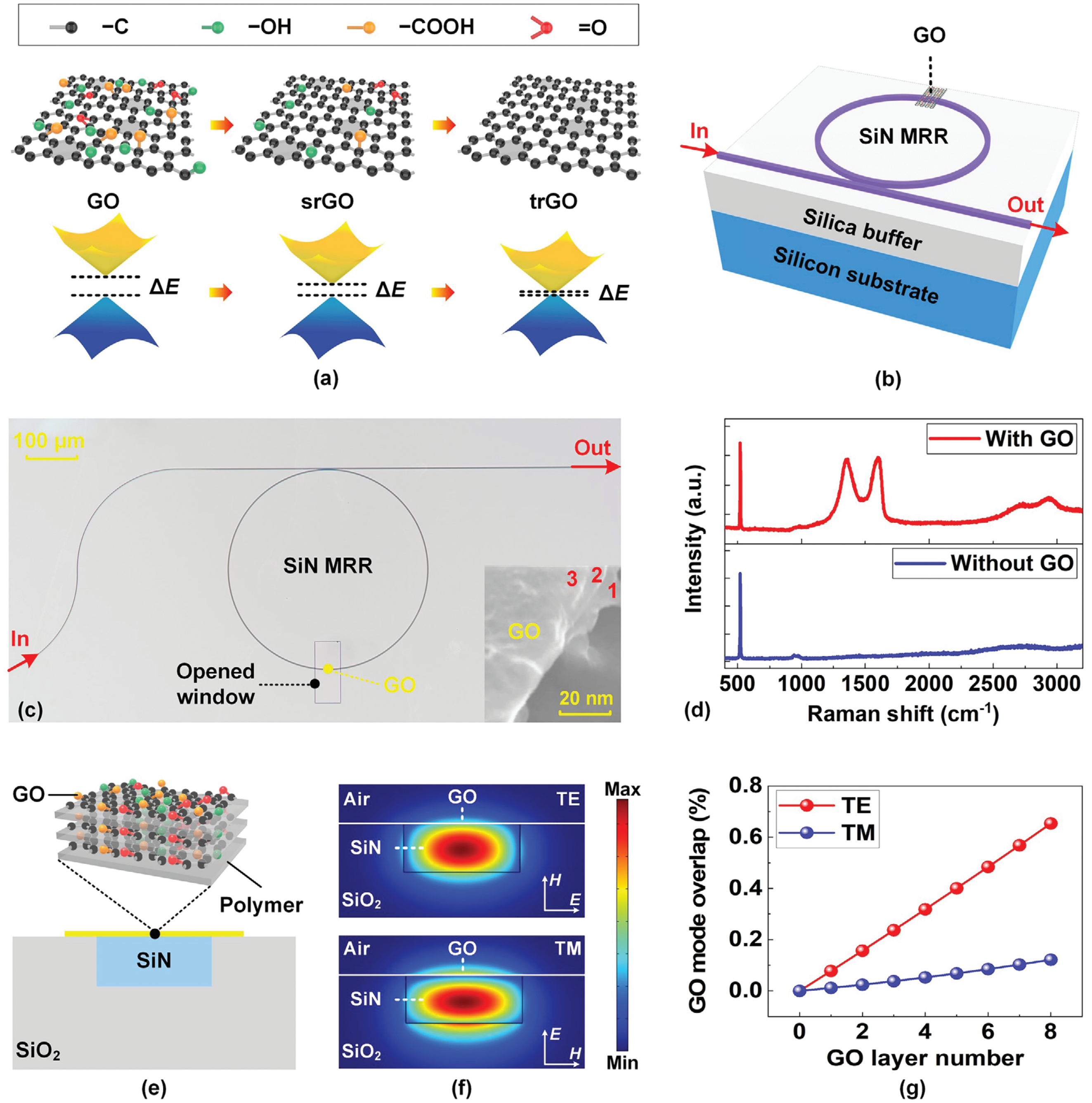

Figure 1. a) Schematics of atomic structures and bandgaps of graphene oxide (GO), semi-reduced GO (srGO), and totally reduced GO (trGO). b) Schematic of a GO-coated silicon nitride (SiN) microring resonator (MRR). c) Microscopic image of a fabricated SiN MRR coated with 3 layers of GO. Inset shows a scanning electron microscopy (SEM) image of the layered GO film, where numbers (1–3) refer to the number of layers for that part of the image. d) Measured Raman spectra of a SiN chip without GO and coated with 1 layer of GO. e) Schematic illustration of cross section and f) corresponding TE and TM mode profiles for the hybrid waveguide with 3 layers of GO. Inset in (e) illustrates the layered GO film fabricated by self-assembly. g) Mode overlap with GO versus GO layer number for both TE and TM polarizations of the hybrid waveguides.

calculated based on mode simulations of the hybrid waveguide at 1550 nm. Due to the difference in volume between the bulk SiN waveguide and the ultrathin 2D GO films, over 88% of light power is confined within the SiN waveguide, and the GO mode overlap is < 1%. For both TE and TM polarizations, the GO mode overlap increases with the GO layer number, mainly resulting from the increase in the GO film thickness. The GO mode overlap for TE polarization is higher than that for TM polarization. Given that the GO film has much higher light absorption compared to the SiN waveguide, a stronger mode overlap with GO leads to a higher propagation loss for the GO-SiN hybrid waveguide.

3. Refractive Indices and Extinction Coefficients

By using the fabricated MRRs coated with 2D GO films, we first characterize the refractive indices (n's) and extinction coefficients (k's) of the GO films with different thicknesses or after experiencing different degrees of reduction. For all the experiments performed in this section, we employed SiN MRRs with a radius of ≈200 µm. The length of the coated GO films, which was approximately equal to the width of the opened window in the silica cladding, was ≈50 µm. Light coupling to the fabricated devices was achieved by using lensed fibres that were butt-coupled to inverse-taper couplers located at both ends of the bus waveguides. The fibre-to-chip coupling loss was ≈4 dB per facet. We also employed a polarization controller (PC) to adjust the polarization of the input light and characterized the n, k values for both TE and TM polarizations.

Figure 2a shows the measured transmission spectra of a SiN MRR coated with 1−3 layers of GO for both TE and TM polarizations. The corresponding results for the uncoated SiN MRR (GO-0) are also shown for comparison. In order to minimize the wavelength shift induced by thermo-optic effects, the transmission spectra were measured by scanning the wavelength of an input continuous-wave (CW) light with a low power of ≈0 dBm. Unless otherwise specified, the input power in our following discussion refers to the power coupled to the MRRs after excluding the fibre-to-chip coupling loss. Compared to the uncoated SiN MRR, the GO-coated MRRs exhibited resonance redshifts, which became more significant as the GO layer number increased. This indicates the variation in the waveguide effective refractive index caused by the GO films. On the other hand, the GO-coated MRRs exhibited decreased extinction ratios (*ER*s, defined as the ratio of the maximum to the minimum transmission) compared to the uncoated MRR, and the *ER* decreased for an increased GO layer number. This reflects that the presence of the GO films also resulted in changes to the waveguide propagation loss.

Figure 2b shows the measured transmission spectra of a SiN MRR coated with 1 layer of GO for both TE and TM polarizations. We measured the transmission spectra for the same MRR by scanning a CW light with a power of ≈0 dBm (i.e., the same as that in Figure 2a). Before measuring the transmission spectra, the integrated chip was heated on a hot plate for 15 min at various temperatures T_R ranging from ≈50 to 200 °C, followed by recording the corresponding Raman spectra as shown in Figure 2c. At T_R = ≈50 °C, the Raman spectrum did not exhibit significant differences as compared to the initial unheated condition, reflecting that there were no significant changes in GO's properties. Whereas for T_R = ≈100 °C and ≈200 °C, a decrease in the intensity ratio of the D to G peaks (I_D/I_G) was observed in the Raman spectra, with the decrease being more significant at T_R = ≈200 °C. This indicates that there was a permanent reduction of GO after the heating process, and a higher degree of reduction was achieved at T_R = ≈200 °C. We did not further increase T_R beyond 200 °C because the polymer layers within the GO films could not withstand temperatures in this range.

In Figure 2b, the transmission spectrum of the MRR after heating at T_R = ≈50 °C showed negligible difference compared to that of the unheated MRR at room temperature, further confirming that there was no permanent reduction of GO at this temperature. Whereas for $T_R \geq 100$ °C, the MRR exhibited a significantly decreased *ER*, and the decrease became more pronounced as T_R increased. Given that reduced GO has higher light absorption than unreduced GO,[25] these results also show agreement with those in Figure 2c and provide further evidence for the permanent reduction of GO at these temperatures. In addition, we observed very slight redshifts in the resonance wavelength for $T_R \geq 100$ °C. This reflects that the reduction of GO also resulted in slight changes in the effective refractive index of the waveguide.

Figure 2d shows n, k values of the layered GO films, which were obtained by using the scattering matrix method[41] to fit the measured transmission spectra in Figures 2a,b. The refractive index of SiN was ≈1.9902 at 1550 nm, which was obtained by fitting the measured spectra for the uncoated SiN MRR. To improve the accuracy, the slight decrease in the film thicknesses (i.e., ≈0.5 nm for 1 layer of GO at T_R = ≈200 °C, measured by atomic force microscopy) was considered when we calculated the n, k values for reduced GO. In Figure 2d, n slightly decreases as the GO layer number increases, but k shows an opposite trend. The former could be attributed to the presence of more air voids in a thicker GO film, which arose from imperfections during the GO film's fabrication processes. Whereas the latter resulted from an increase in scattering loss due to film unevenness and accumulation of imperfect contact between adjacent layers in a thicker film.

In Figure 2d, both n and k initially exhibited no significant changes for $T_R \leq 50$ °C, but then showed a more noticeable increase with T_R for $T_R \geq 100$ °C. These results reflect the changes in GO's n, k induced by thermal reduction. Since the CW light power used to scan the spectra was not sufficient to induce any significant thermo-optic effects, the changes in n, k were mainly induced by changes resulting from the heating treatment before the measurement. The n, k values for unreduced GO were ≈1.9720 and ≈0.0097, respectively. In contrast, the corresponding values for the reduced GO at T_R = ≈200 °C were ≈2.2000 and ≈0.3557. The change in n, i.e., Δn = ≈0.2280, is over 1 order of magnitude larger than conventional bulk refractive materials.[42] In addition, k also changes from ≈0.0097 to ≈0.3557 – an increase of over 36-fold. The broad variation ranges for both n and k are critical for engineering and manipulation of the phase and amplitude response of many GO devices, such as optical lenses and holographic displays.[32,43]

The results in Figure 2d also reveal the differences in the n, k values between TE and TM polarizations. For all different GO layer numbers and T_R's, the GO film exhibits higher values of n, k for TE polarization than TM polarization. This is mainly caused by the intrinsic material anisotropy of the 2D GO films with atomically thin thicknesses, which leads to distinctive responses for light in different polarization states. In the GO-SiN MRR, the TE polarization supports in-plane light-GO interaction, which is much stronger as compared to the out-of-plane interaction supported by TM polarization. For 1 layer of GO, the n, k values for TE polarization were n_{TE} = ≈1.9720 and k_{TE} = ≈0.0097, respectively. In contrast, the corresponding values for TM polarization were n_{TM} = ≈1.9000 and k_{TM} = ≈0.0032. The large difference in the n, k values between TE and TM polarizations reflects the significant material anisotropy of the 2D GO films, which has been demonstrated useful for realizing liquid crystal display devices and optical polarizers.[29,44]

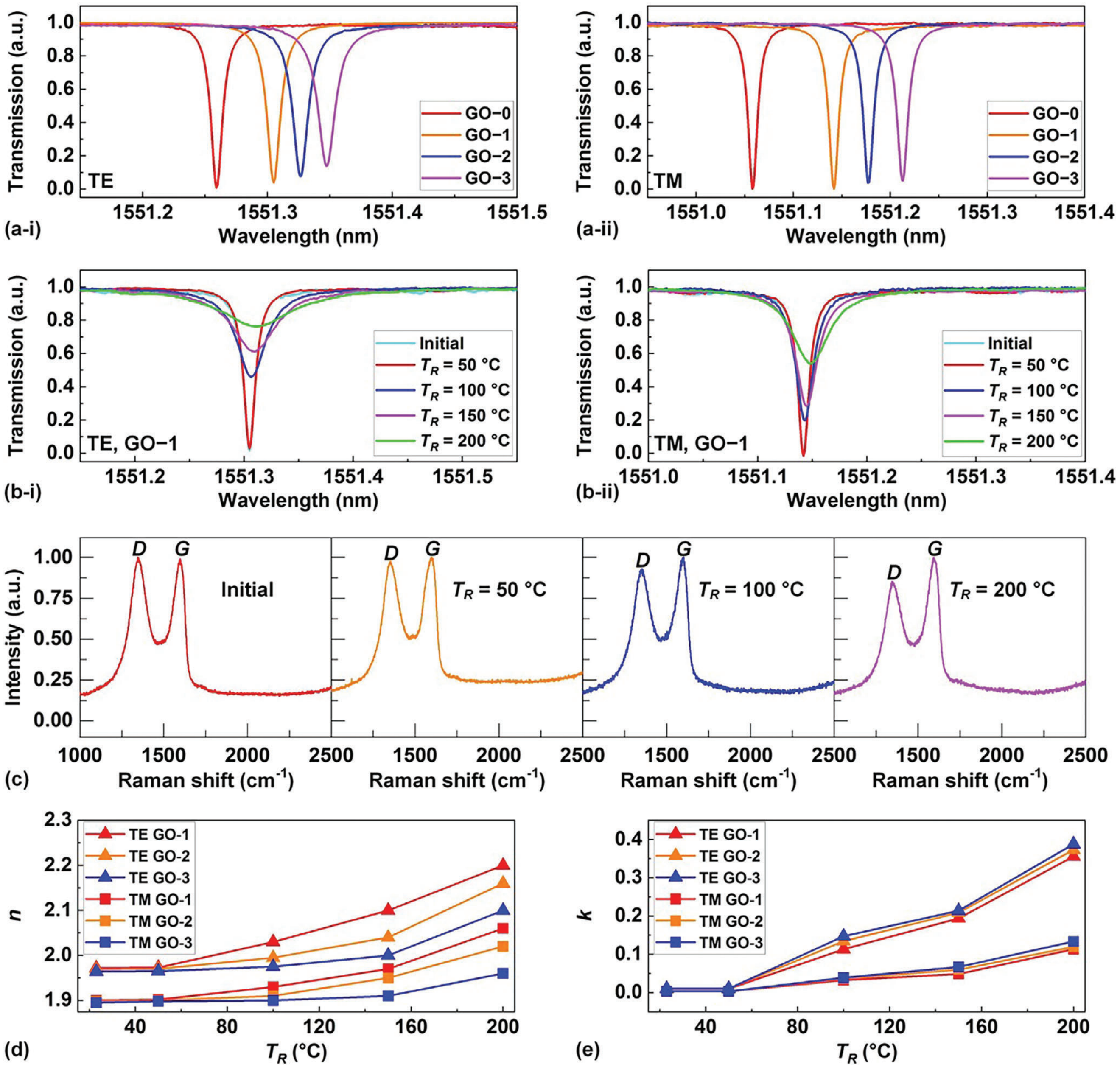

Figure 2. a) Measured (i) TE- and (ii) TM-polarized transmission spectra of the hybrid MRRs with 1–3 layers of GO. The corresponding results for the uncoated SiN MRR (GO-0) are also shown for comparison. b) Measured (i) TE- and (ii) TM-polarized transmission spectra of a hybrid MRR with 1 layer of GO. The GO-SiN chip underwent heating at various temperatures T_R prior to the measurement of its transmission spectra. The corresponding results for the chip at room temperature before heating (initial) are also shown for comparison. c) Raman spectra of the GO-SiN chip in (b), which were measured at room temperature (initial) and after heating at different T_R. d) Extracted (i) refractive index n and (ii) extinction coefficient k of the films including 1–3 layers of GO versus T_R for both TE and TM polarizations.

From a material perspective, the presence of both the polarizable bonds and the π-conjugation of carbon network in GO could contribute to its polarization-sensitive properties, including not only the n, k discussed here but also other properties addressed in subsequent sections. As mentioned previously, in GO the carbon network is decorated with various OFGs. Previous studies have found that the bonds for carbonyl (C = O) and hydroxyl (–OH) groups in GO were highly polarizable.[45,46] This is mainly caused by a higher electronegativity of oxygen atoms compared to carbon and hydrogen atoms, which leads to an increase in the electric dipole moment. On the other hand, the large π-conjugated domains of the carbon network can enhance the polarization sensitivity due to the delocalization of π-electrons, which leads to increased electric dipole moments and a more significant shift in the electron density.[47,48] In GO that contains both sp^2 and sp^3 hybridization, the polarizable bonds with sp^2 hybridization coexist

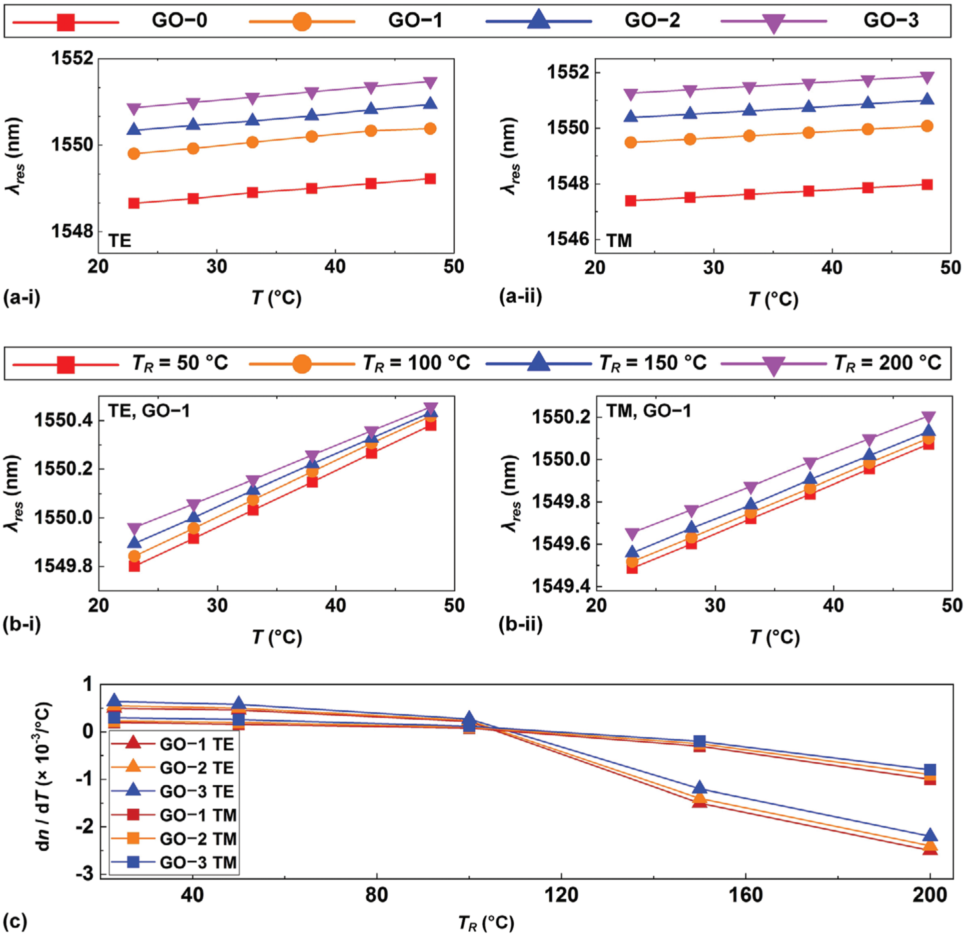

Figure 3. a) Resonance wavelength λ_{res} versus chip temperature T (changed via a temperature controller) for the hybrid MRRs with 1–3 layers of GO. (i) and (ii) show the results for TE and TM polarizations, respectively. The corresponding results for the uncoated SiN MRR (GO-0) are also shown for comparison. b) λ_{res} versus T for the hybrid MRR with 1 layer of GO. The GO-SiN chip underwent heating at temperatures T_R ranging from ≈50 to 200 °C prior to the measurement. (i) and (ii) show the results for TE and TM polarizations, respectively. c) Extracted thermo-optic coefficient dn/dT of the films including 1–3 layers of GO versus T_R for both TE and TM polarizations.

with the π-conjugation of carbon network with sp^3 hybridization, and the reduction of GO leads to an increased portion for the latter. This could be a possible reason for the slight difference in the ratios of $n_{\mathrm{TE}}/n_{\mathrm{TM}}$ and $k_{\mathrm{TE}}/k_{\mathrm{TM}}$ between GO and reduced GO.

4. Thermo-Optic Coefficients

In this section, we use the fabricated GO-SiN MRRs to characterize the thermo-optic coefficients of the GO films with different thicknesses or with different degrees of reduction. The thermo-optic coefficient is a fundamental parameter that indicates the change in the refractive index of a material with variations in environmental temperature.

For the experiments performed in this section, we employed 2 types of SiN MRRs. The first type had a radius of ≈56 µm, with the silica upper cladding of the integrated chip being removed by using highly selective chemical-mechanical polishing to enable coating the entire MRR with GO films. The second type was the same as those used in Section 3, which had a radius of ≈200 and ≈50-µm-long opened windows. We chose the first type of MRRs for all devices, except for those with GO layer number $N \geq 2$ and reduction temperature $T_R \geq 150$ °C. This is because the first type can magnify the difference in the measured wavelength shifts caused by GO films as compared to the second type. However, for the devices with both large GO film thicknesses and high GO reduction degrees, the *ER* becomes too low, which makes it difficult to precisely characterize the wavelength shift. We measured the transmission spectra of the GO-SiN MRRs by scanning the wavelength of a CW light with an input power of ≈0 dBm. For the MRRs entirely covered by GO films in this section and Section 5, the input power in our discussion also excludes the GO-induced propagation loss along the input waveguide. To adjust the temperature of the GO-SiN MRRs, the fabricated chip was placed on a temperature controller with a minimum resolution of ≈0.1 °C.

Figure 3a shows the measured resonance wavelength λ_{res} versus chip temperature T for the SiN MRRs coated with 1–3 layers of GO. We show the results for both TE and TM polarizations, and the corresponding results for the uncoated SiN MRR (GO-0) are also shown for comparison. To prevent changes in GO film properties caused by thermal reduction, the chip temperature was not raised beyond 50 °C. As can be seen, all the MRRs exhibited a redshift in their resonance wavelengths, albeit at slightly different rates. For instance, the TE-polarized λ_{res} of the uncoated MRR redshifted at a rate of ≈22.9 pm $°C^{-1}$, in contrast to ≈23.3 pm $°C^{-1}$ for the TE-polarized λ_{res} of the hybrid MRR with 1 layer of GO. Figure 3b shows the measured λ_{res} versus T for a hybrid MRR with 1 layer of GO. Similar to that in Figure 2b, before conducting the measurement, the GO-SiN chip was heated at various T_R on a hot plate for 15 min. As a result, the measured redshifts in Figure 3b can be used to calculate the thermo-optic coefficients of reduced GO at various degrees of reduction.

Figure 3c shows the thermo-optic coefficient $\mathrm{d}n/\mathrm{d}T$ of the films including 1–3 layers of GO versus T_R for both TE and TM polarizations. The values of $\mathrm{d}n/\mathrm{d}T$ were calculated based on the results in Figures 3a,b, using the relationship between the resonance wavelengths and the waveguide effective refractive index given by:

$$n_{eff} \times 2\pi \,/\lambda_m \times L = m \times 2\pi \tag{1}$$

where n_{eff} is the effective refractive index of the hybrid waveguide, L is the circumference of the SiN MRR, and λ_m is the resonance wavelength of the mth resonance.

In Figure 3c, as T_R increases, the value of $\mathrm{d}n/\mathrm{d}T$ changes from positive to negative for all 3 GO layer numbers. For 1 layer of unreduced GO in TE polarization, the value of $\mathrm{d}n/\mathrm{d}T$ is $\approx 0.5 \times 10^{-3}$ $°C^{-1}$, in contrast to $\approx -2.5 \times 10^{-3}$ (m °C)$^{-1}$ for reduced GO at T_R = ≈200 °C with the same GO layer number and polarization. These results reflect interesting changes in GO's thermo-optic coefficient induced by thermal reduction. The thermo-optic coefficient of unreduced GO is higher than silicon ($\approx 1.8 \times 10^{-4}$/°C.[49]) Given that most materials have positive values of thermo-optic coefficients, the negative thermo-optic coefficients exhibited by reduced GO can be utilized to mitigate thermal drift induced by temperature variation and develop athermal devices.[41,50] The large variation range for the thermo-optic coefficient also increases the range of functionalities and devices that can be developed.

We also note that thicker GO films showed higher values of $\mathrm{d}n/\mathrm{d}T$ in Figure 3c, which can be attributed to diminished thermal dissipation in them, especially considering the presence of polymer layers between the GO layers. Similar to that in Figure 2c, the GO film exhibits a significant difference in the values of $\mathrm{d}n/\mathrm{d}T$ for TE and TM polarizations. For unreduced GO with positive values of $\mathrm{d}n/\mathrm{d}T$, the $\mathrm{d}n/\mathrm{d}T$ for TE polarization is higher than that for TM polarization. Whereas for reduced GO at T_R = ≈200 °C with negative values of $\mathrm{d}n/\mathrm{d}T$, the $\mathrm{d}n/\mathrm{d}T$ for TE polarization is lower than that for TM polarization. These phenomena can also be attributed to the stronger in-plane light-GO interaction supported by TE polarization compared to the out-of-plane interaction supported by TM polarization. We also calculated the $\mathrm{d}n/\mathrm{d}T$ values of SiN based on the measured results for an uncoated SiN MRR, which were $\approx 4.80 \times 10^{-5}$ $°C^{-1}$ and $\approx 4.76 \times 10^{-5}$ $°C^{-1}$ for TE and TM polarizations, respectively. These values show agreement with those reported in Ref. [51], and the close resemblance between the coefficients for TE and TM polarizations reflects that SiN does not exhibit significant anisotropy in terms of its thermo-optic coefficient. By using the same method as in Refs. [52,53], we also characterized the response times of refractive index change induced by the thermo-optic effect for both GO and reduced GO (at T_R = ≈200 °C). Both of them were on the order of $\approx 10^{-4}$ s, with the response for reduced GO being faster than that for GO, likely due to its higher thermal conductivity (which will be discussed in Section 5).

5. Thermal Conductivities

Thermal conductivity is a parameter that defines a material's ability to conduct heat, which is of fundamental importance in modelling heat transfer for thermal management.[18] In this section, we characterize the thermal conductivities of the layered GO films with different thicknesses and degrees of reduction by using the fabricated GO-SiN MRRs.

For the experiments performed in this section, we also employed the 2 types of SiN MRRs as those used in Section 4. We used 2 CW lights to measure the transmission spectra of the GO-coated MRRs. The first one served as a pump injecting into one of the MRR's resonances. The wavelength of this input CW light was slightly tuned from blue to red around the resonance until it reached a steady thermal equilibrium state with stable output power. After this, the second CW light, with a constant power of ≈0 dBm, was employed as a low-power probe to scan the MRR's transmission spectrum. Compared to directly employing a high-power CW light to scan the spectra, our approach can minimize the asymmetry in the measured resonance lineshape resulting from optical bistability (which will be discussed in Section 7), thus allowing more precise measurement of the resonance wavelength shifts. We measured the resonance wavelength shifts of the fabricated GO-SiN MRRs for various input pump powers and extracted the thermal conductivity by fitting the wavelength shift with theoretical simulations.

Figure 4a shows the measured resonance wavelength shift $\Delta\lambda$ versus the power of the CW pump P_p for the uncoated SiN MRR and the hybrid MRR with 1 layer of GO. We chose the range of $P_p \leq$ ≈200 mW because, within this range, there were no observable changes in the ER of the hybrid MRR compared to that measured at $P_p = 0$. This implies that GO film did not experience thermal reduction induced by the CW pump power. For both the uncoated and the hybrid MRRs, $\Delta\lambda$ increases gradually for small $P_p < 50$ mW, and then increases more significantly as P_p further increases. As P_p increases, the difference in $\Delta\lambda$ between the uncoated and hybrid MRRs also becomes more significant.

In our modelling, the steady-state temperature distributions in the waveguide cross-section were simulated using commercial finite-element multi-physics software (COMSOL Multiphysics) to solve the heat equation described by *Fourier*'s law as:[18]

$$-\nabla \cdot (K\nabla T) = q \tag{2}$$

where q is the heat flux density, K is the material's thermal conductivity, ∇T is the temperature gradient, and ∇ acting on the vector function $K\nabla T$ is the divergence operator. The heat flux intensity q in the MRR was calculated by:[54]

$$q = \frac{P \times BUF \times R}{w \times h \times l} \tag{3}$$

where P is the input CW power that equals to P_p (neglecting the small difference induced by the low-power probe), R is the

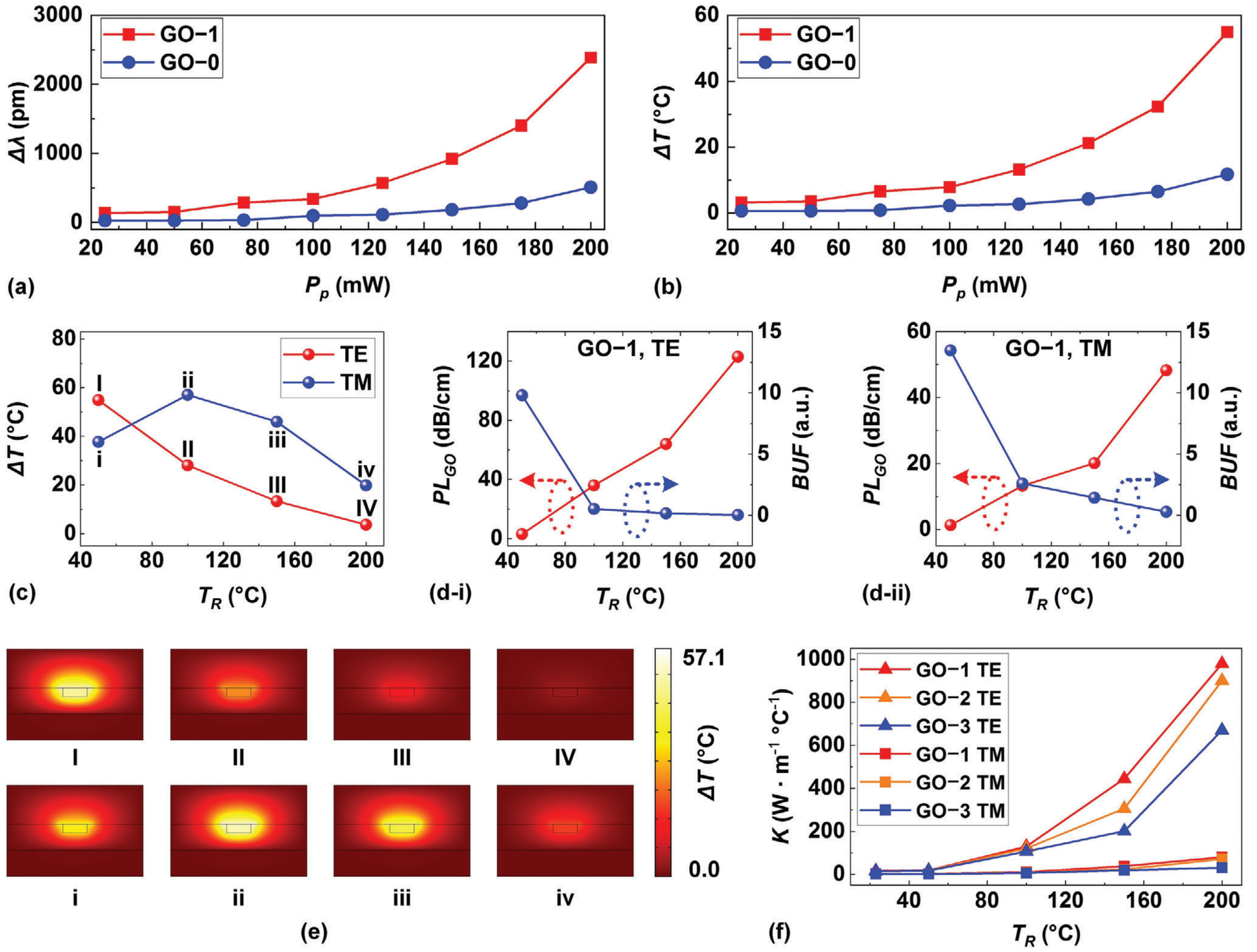

Figure 4. a) Measured resonance wavelength shift $\Delta\lambda$ versus input continuous-wave (CW) pump power P_p for the uncoated SiN MRR (GO-0) and the hybrid MRR with 1 layer of GO (GO-1). b) Calculated temperature changes at the waveguide core ΔT versus P_p for the uncoated SiN MRR (GO-0) and the hybrid MRR with 1 layer of GO (GO-1). c) Calculated ΔT for the hybrid MRR with 1 layer of GO after the chip was heated at various temperatures T_R. d) Calculated GO-induced propagation loss PL_{GO} and intensity build-up factor BUF of the hybrid MRR with 1 layer of GO versus T_R. (i) and (ii) show the results for TE and TM polarizations, respectively. e) Simulated temperature distributions in the waveguide cross-section for the hybrid MRR with 1 layer of GO. (I) – (IV) and (i) – (iv) correspond to the different points in (c). f) Extracted thermal conductivity K of the films including 1–3 layers of GO versus T_R for both TE and TM polarizations. In (c) – (e), P_p = ≈200 mW, at which there were no observable changes in the extinction ratios of the hybrid MRRs as compared to those measured at $P_p = 0$. In the thermal simulation, the initial temperature was assumed to be at room temperature of 23 °C.

conversion efficiency that determines the amount of light power converted into heat, w, h, and l are the waveguide width, height, and length, respectively, and BUF is the MRR's intensity build-up factor that can be expressed as:[55]

$$BUF = \frac{\left(1 - t^2\right) a^2}{1 - 2ta + t^2 a^2} \tag{4}$$

where a is the round-trip amplitude transmission, and t is the field transmission coefficient of the directional coupler. The values of a and t were obtained by fitting the measured spectrum of the MRR.

Based on the measured resonance wavelength shift in Figure 4a, we first calculated the variation in the waveguide effective refractive index and extracted the change in the refractive index of SiN (Δn_{SiN}) based on optical mode simulations (e.g., Δn_{SiN} = ≈5.86 × 10^{-4} at P_p = ≈200 mW). Next, by dividing Δn_{SiN} by the thermo-optic coefficient of SiN (i.e., ≈4.80 × 10^{-5}/°C, obtained from the experiments in Section 4), we derived the change in temperature ΔT at the waveguide core (e.g., ΔT = ≈12.2 °C at P_p = ≈200 mW). We calculated ΔT values for the uncoated and the GO-coated MRR and plotted them as functions of P_p in Figure 4b. In Figure 4a, the GO-coated MRR exhibited a more significant redshift compared to the uncoated MRR. This indicates that the GO-coated MRR experienced a more significant phase shift resulting from the heat generated by the GO films. This is also reflected by the higher values of ΔT for the GO-coated MRR in Figure 4b.

After measuring the resonance wavelength shifts of a hybrid MRR with 1 layer of GO following the heating of the chip at various T_R, we employed the same method as in Figure 4b to calculate the corresponding ΔT. Figure 4c shows the calculated ΔT versus T_R for both TE and TM polarizations. For comparison, the input pump power was kept the same as $P_p = \approx 200$ mW, at which there were no observable changes in the *ER*s of these MRRs as compared to those measured at $P_p = 0$. For TE polarization, ΔT decreases with increasing T_R. For TM polarization, ΔT initially rises with T_R and then starts to decline after reaching peak values at $T_R = \approx 100$ °C. To delve deeper into the underlying reasons for this interesting phenomenon, we calculated the GO-induced propagation loss PL_{GO} and the *BUF* of these MRRs, and depicted them in Figure 4d. As can be seen, PL_{GO} increases with T_R for both polarizations, while *BUF* exhibits an opposite trend. This is not surprising given the fact that the reduced GO at $T_R \geq 100$ °C has a higher light absorption than unreduced GO. Since the light absorbed by the GO film is converted to heat, the increased light absorption for reduced GO also leads to a higher value of R in Equation (3). Hence, the observed phenomena in Figure 4c result from the trade-off between a decreased *BUF* and an increased R in Equation (3) as T_R increases. For TE polarization, ΔT exhibits a monotonic decrease mainly due to the dramatic decrease in the *BUF*, which cannot be offset by the relatively small increase in R.

Based on the calculated ΔT values for the GO-coated MRR, we further extracted the thermal conductivities of the GO films by fitting the ΔT values with those obtained from thermal simulations based on COMSOL Multiphysics. In our simulations, the GO film in the GO-coated MRR was regarded as an additional heat source that absorbed light power and generated heat, which in turn caused a temperature change, ΔT, in the underlying SiN waveguide. The heat flux densities in the GO films and the SiN waveguide were calculated individually based on Equation (3). By fitting the ΔT values for the uncoated SiN MRR, we obtained $R = \approx 0.40\%$ for the uncoated SiN waveguide. The values of R for the GO films were calculated based on the linear loss of the GO films obtained in Section 3, assuming that all the light absorbed by GO – equivalent to the additional loss induced by GO – was converted to heat. The values of K for each of the material regions were also specified (*e.g.*, $K_{\text{SiN}} = \approx 29.0$ W (m °C)$^{-1}$, $K_{\text{SiO2}} = \approx 1.4$ W (m °C)$^{-1}$, $K_{polymer} = \approx 0.25$ W (m °C)$^{-1}$, and $K_{air} = \approx 0.03$ W (m °C)$^{-1,}$[54,56]) with the exception of the GO film that needed fitting. The initial temperature T_0 was set to 23 °C, which was the ambient temperature during our experiments.

Figure 4e shows the simulated temperature distributions in the waveguide cross-section for the hybrid MRR with 1 layer of GO, where (I) – (IV) and (i) – (iv) correspond to the different points in Figure 4c. Figure 4f shows the thermal conductivity K of the films including 1–3 layers of GO versus T_R for both TE and TM polarizations. For the devices entirely coated with GO films, the results were obtained by fitting the measurements at $P_p = \approx 200$ mW. For the devices with patterned GO films (i.e., for $N \geq 2$ and $T_R \geq 150$ °C), the results were obtained by fitting the measurements at $P_p = \approx 40$ mW. This is because these MRRs have higher *BUF* values that would lead to changes in the *ER* at a relatively low P_p. For the devices with patterned GO films, the hybrid MRR was divided into uncoated and GO-coated segments. For the uncoated segment, since the presence of GO increased the round-trip loss of the MRR and hence reduced the *BUF*, the heat flux density and temperature increase in the uncoated segment were lower compared to those for the uncoated SiN MRR. Assuming that R for the uncoated segment remains consistent with that obtained from the uncoated MRR, and neglecting the slight temperature variation induced by heat transfer between the uncoated and GO-coated segments, we obtained the ΔT for the uncoated segment in the hybrid MRR via thermal simulations (using q calculated based on Equation (3)). Using this ΔT, we further calculated the additional phase shift along the uncoated segment based on Equation (1). This, together with the measured resonance wavelength shift for the hybrid SiN MRR, allows us to calculate the additional phase shift along the GO-coated segment and the corresponding ΔT in this segment.

In Figure 4f, a thicker GO film exhibits a lower value of K, further confirming its lower thermal dissipation property. For 1 layer of unreduced GO, the value of K is ≈16.3 W (m °C)$^{-1}$ for TE polarization. This value is higher than that reported in Ref. [57] (i.e., ≈2.0 W (m °C)$^{-1}$) for GO films with greater thicknesses (e.g., ≈143 nm). The decrease in the thermal conductivity with increasing film thickness can be attributed to more significant scattering of phonons from the film surface caused by film unevenness, lattice impurities, and structural defects within thicker films.

Compared to unreduced GO, higher values of K are obtained for reduced GO at $T_R \geq 100$ °C, with K increasing as the degree of reduction increases. For 1 layer of reduced GO at $T_R = \approx 200$ °C, the value of K is ≈979 W (m °C)$^{-1}$ for TE polarization, which is more than 27 times that of comparable unreduced GO. These results reflect that the reduced GO films possess superior heat conduction properties, which can be attributed to the diminished presence of the OFGs that induce phonon-scattering from the film surface. We also note that the value of ≈979 W (m °C)$^{-1}$ is ≈5 times lower than the reported value for graphene,[58] which is due to the fact that the GO film at $T_R = \approx 150$ °C was still not fully reduced and the existence of polymer layers with much lower thermal conductivity in our GO films.

We also note that the TE polarization exhibited higher values of K than the TM polarization for all 3 GO layer numbers in Figure 4f. This indicates that the GO films also exhibit anisotropic thermal conductivity – similar to the anisotropy observed in their refractive index, extinction coefficient, and thermo-optic coefficient. The ratios between the in-plane and out-of-plane thermal conductivities are ≈6.5 for 1 layer of unreduced GO and ≈12.2 for 1 layer of reduced GO at $T_R = \approx 200$ °C. A maximum ratio of ≈21.3 was obtained for 3 layers of reduced GO at $T_R = \approx 200$ °C. We note that in Ref. [59] a considerably higher ratio of ≈675 was achieved for thick (≈40 µm) reduced GO films annealed at ≈1000 °C. In these films, the formation of "air pockets" with limited thermal transport capability between the GO layers strongly hindered out-of-plane thermal transport but did not significantly affect the in-plane thermal conduction. In contrast to this ratio achieved through engineering the fabrication processes of thick GO films, our calculated ratios more accurately reflect inherent anisotropy in the thermal conductivities of 2D GO films.

6. GO Reduction Induced by Localized Photo-Thermal Effects

For the experiments in Section 5, the input CW pump power P_p was maintained below a specific threshold to ensure that there were no obvious changes in the *ER*s of the hybrid MRRs compared to that measured at $P_p = 0$. As a result, the GO films remained unaffected by thermal reduction induced by the CW pump power. In this section, we further increase P_p to be above the threshold and characterize the changes in the *ER*s of the hybrid MRRs induced by thermal reduction of the GO films. Compared to the thermal reduction of GO caused by heating the entire chip on a hotplate (at various T_R) in previous experiments, using the CW pump power to trigger the thermal reduction of GO leads to localized effects, which can cause dynamic changes in the GO film properties. For the experiments in this section, we employed the same experimental method as that in Section 5. The employed MRRs were the same as those in Section 3, which had a radius of ≈200 µm and opened windows with a length of ≈50 µm. Compared to the MRRs entirely coated with GO films, the MRRs with patterned GO films have lower round-trip loss and higher *BUF*s, which can more easily induce the photo-thermal effects in the GO films by leveraging the resonance enhancement provided by the MRRs.

Figure 5a shows the measured *ER* versus P_p for the hybrid MRR with 1 layer of GO. In (i) and (ii), we show the results for TE and TM polarizations, respectively. In Figure 5a(i), the *ER* remained constant at ≈14.0 dB for $P_p \leq 40$ mW. However, an obvious decrease in the *ER* was observed for $P_p > 40$ mW, indicating an increased loss in the hybrid MRR induced by thermal reduction of the GO film. In the hybrid MRR, localized heating occurs due to optical absorption, which leads to a range of photo-thermal effects within the GO film such as self-heating, thermal dissipation, and photo-thermal reduction. Upon reaching the power threshold, the reduction of GO can be initiated when the thermal heating initiates a deoxygenation reaction in GO. The reduced GO with higher light absorption increased the loss in the MRR, consequently lowering its *ER*. We also observed an interesting phenomenon – when P_p exceeded the lower power threshold of $P_{thres1} = \approx 40$ mW but remained below the higher power threshold of $P_{thres2} = \approx 72$ mW (which is highlighted by the blue shaded area), the *ER* of the hybrid MRR returned to its initial value of ≈14.0 dB upon switching off the CW pump. This reversibility reflects the instability of the reduced GO induced by photo-thermal effects, which can easily revert to the original unreduced state once it has cooled down in an oxygen-containing ambient. The reversible GO reduction within the MRR enables dynamic tuning of the MRR's *ER*, which can be useful for potential applications such as optical switches and power limiting.[60,61] In Ref. [52], we have characterized the response time of reversible reduction of 2D GO films induced by photo-thermal effects, which was on the order of $\approx 10^{-4}$ s and showed an agreement with typical thermal-optic responses.[18]

As P_p continued to rise above ≈72 mW, there were permanent changes in the *ER* after switching off the CW pump. This occurred because the temperature rise resulting from localized heating caused by the CW pump reached a level where it permanently fractured the chemical bonds between the OFGs and the carbon network. This led to a lasting alteration in the atomic structure of GO and hence its properties. For $P_p > 110$ mW, the *ER* nearly approaches 0, indicating a substantial increase in loss induced by the highly reduced GO. It should be noted that for $P_p > \approx 72$ mW, there was an increase in the *ER* after turning off the CW pump, although the *ER* could not return to the initial value of ≈14.0 dB. At $P_p = \approx 160$ mW, there was still a slight increase in the *ER* (≈0.2 dB) when the CW pump was off, reflecting the fact that the highly reduced GO at this power level was not yet fully reduced.

In Figure 5a(i), the dashed horizontal lines indicate the measured *ER*s for the hybrid MRR with 1 layer of GO after the chip was heated on a hotplate at various T_R (i.e., the same as those in Figure 2b, which were measured by scanning a CW light with a power ≈1 mW). These lines were plotted to compare the performance between localized heating using a CW pump and uniform heating of the entire chip via a hotplate. As can be seen, despite using different methods to reduce the GO film, similar *ER*s can be achieved for the hybrid MRRs with GO films reduced to different degrees.

For TM polarization in Figure 5a(ii), reversible GO reduction was observed for P_p within the range of ≈82–123 mW. Compared to TE polarization, the lower power threshold P_{thres1} is higher and the power range for reversible reduction is larger for TM polarization. This reflects the relatively weak photo-thermal effects for TM polarization due to the significant anisotropy of the GO film, aligning with the experimental results in previous sections.

Figures 5b,c show the corresponding results for the hybrid MRRs with 2 and 3 layers of GO, respectively. For the hybrid MRR with 2 layers of GO, reversible GO reduction was observed for P_p within the range of ≈36-58 mW, and for the hybrid MRR with 3 layers of GO, it was observed for P_p within the range ≈32–47 mW. Compared to the results in Figure 5a, the hybrid MRR with a thicker GO film shows a decreased P_{thres1} and a smaller power range, reflecting the more significant photo-thermal effects in them.

In Figure 5d, we provide a schematic to illustrate the changes in GO's atomic structure as P_p increases in Figures 5a–c, where I – IV represent 4 different stages at different levels of P_p. The atomic structure at stage I corresponds to unreduced GO at the initial status, with no light injected into the MRR. At stage II, P_p was below P_{thres1} – the threshold for initiating a deoxygenation reaction in GO, and there were no obvious changes in GO's atomic structure. At stage III, GO reduction occurred as P_p exceeded P_{thres1}, and it exhibited a reversible behaviour by returning to stage I once the light power was turned off. At stage IV, as P_p increased beyond P_{thres2}, the localized heating became strong enough to permanently alter GO's atomic structure by breaking the chemical bonds between the OFGs and the carbon network.

Since our integrated chip coupling setup (including lensed fibres, fibre coupling stages, charge-coupled device (CCD) cameras, *etc.*) is incompatible with the Raman spectroscopy setup, we cannot directly characterize the photo-thermal reduction of GO in the hybrid MRRs. Instead, we measured the Raman spectra for a GO-coated chip before, during, and after heating at ≈80 °C, and the results are shown in Figure 5e. As can be seen, the intensities of *D* peaks for the Raman spectra measured before and after the heating treatment show negligible differences. In contrast, an obvious decrease in the intensity of the *D* peak was observed during the heating process, showing agreement with those observed for reduced GO in Refs. [62,63]. These results provide further evidence for the reversible reduction of GO at stage III in Figure 5d, which can return to stage I after heating treatment.

In Figure 5, before injecting the CW pump, the hybrid MRRs were coated with unreduced GO films. In **Figure** 6, we further

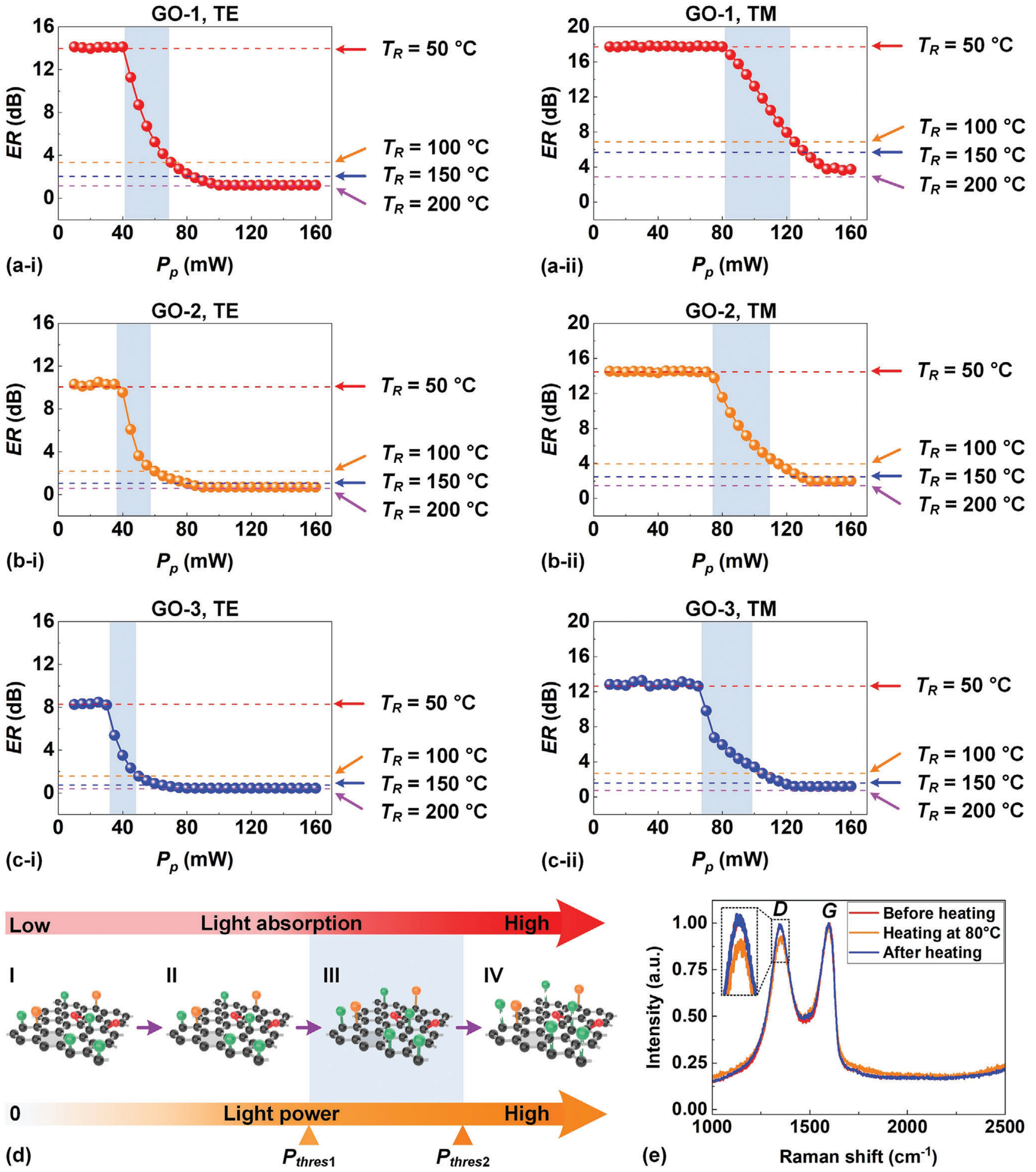

Figure 5. Measured extinction ratio *ER* versus input CW pump power P_p for the hybrid MRRs with a) 1, b) 2, and c) 3 layers of GO. In (a) – (c), (i) and (ii) show the results for TE and TM polarizations, respectively. The dashed horizontal lines indicate the *ER*s for the corresponding MRRs after the chip was heated at various temperatures T_R and measured by scanning a CW light with a power of ≈1 mW. d) Schematic illustration for changes in GO's atomic structure as P_p increases in (a) – (c). I – IV represent 4 stages corresponding to different P_p. P_{thres1} and P_{thres2} represent the power thresholds for initiating GO reduction and causing permanent changes, respectively. In (a) – (d), the blue shaded area indicates the power ranges associated with reversible GO reduction. e) Raman spectra of a GO-coated chip measured before, during, and after heating at ≈80 °C. The different spectra were normalized according to the intensities of the *G* peaks, and the inset shows a zoom-in view around the *D* peaks.

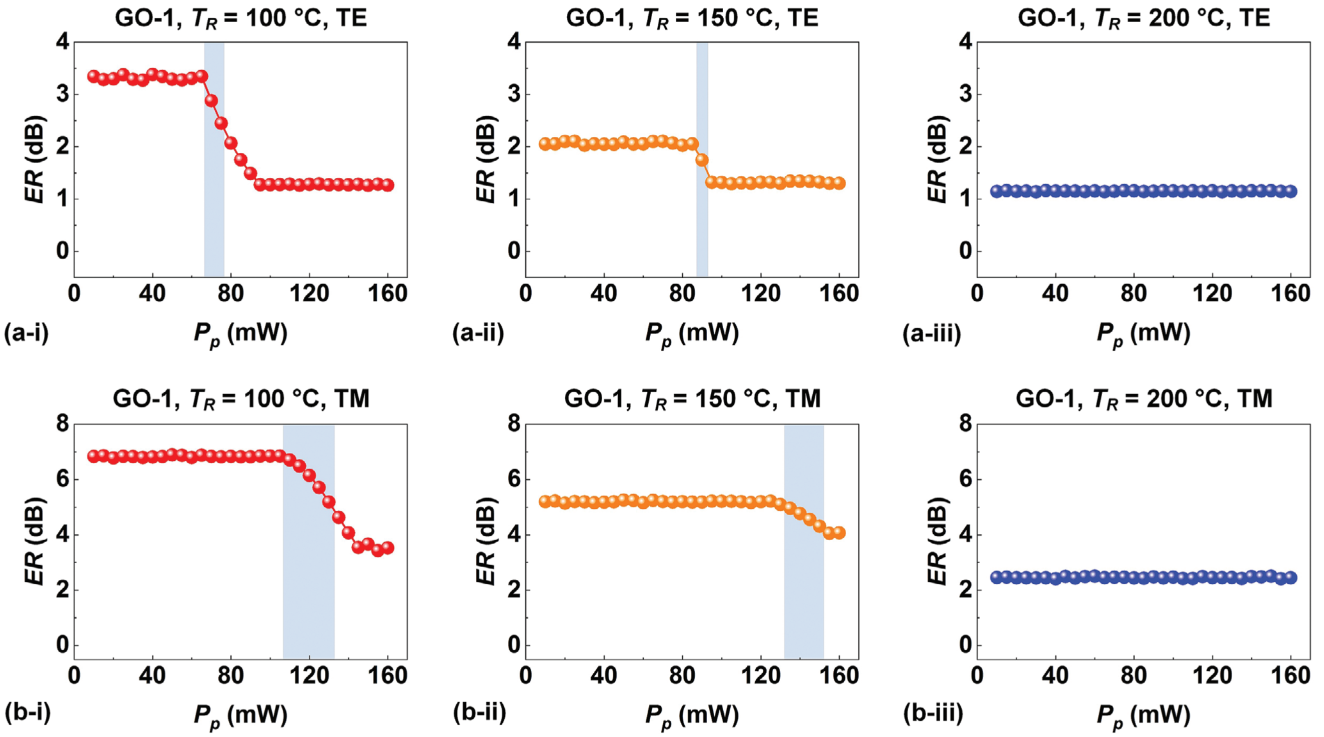

Figure 6. Measured extinction ratio *ER* versus input CW pump power P_p for the hybrid MRR with 1 layer of reduced GO for a) TE and b) TM polarization. In (a) – (b), (i) – (iii) show the results measured after the chip was heated at temperatures of $T_R = \approx 100$ °C, $T_R = \approx 150$ °C, and $T_R = \approx 200$ °C, respectively. The blue shaded areas indicate the power ranges associated with reversible GO reduction.

characterize the performance of the hybrid MRRs with reduced GO films before injecting the CW pump. In Figures 6a,b, we show the measured *ER* versus P_p for the hybrid MRR with 1 layer of reduced GO for TE and TM polarizations, respectively. Prior to injecting the CW pump and measuring the transmission spectra, the chip was heated on a hotplate to obtain reduced GO at different degrees of reduction. In each figure, (i) – (iii) show the results measured after the chip was heated at $T_R = \approx 100$, ≈150, and ≈200 °C, respectively.

For $T_R = \approx 100$ °C in Figure 6a(i), reversible GO reduction was observed for P_p within the range of ≈65–78 mW. Compared to the results for unreduced GO in Figure 5a(i), the P_{thres1} is higher, and the power range is smaller. This indicates that unreduced GO was more easily reduced by the CW pump. In Figure 6a(ii), for reduced GO at $T_R = \approx 150$ °C, reversible GO reduction was observed with an even higher P_{thres1} and in an even smaller range of ≈87–93 mW. For the reduced GO at $T_R = \approx 200$ °C in Figure 6a(iii), no significant changes in the *ER* were observed, indicating that there was no obvious reversible GO reduction for highly reduced GO. These results further confirm that the reversible reduction behaviour becomes less obvious as the degree of reduction increases. Similar to Figure 5, the results for TM polarization in Figure 6b show higher P_{thres1} values and larger ranges for reversible GO reduction compared to the corresponding results for TE polarization in Figure 6a. At $T_R = \approx 200$ °C, there were also no obvious changes in the *ER* for TM polarization.

In **Figure 7**, we compare the reversible GO reduction behaviours in GO-coated SiN MRRs and waveguides. In our measurements, the GO-coated MRRs had a radius of ≈200 µm, and the GO film length was ≈50 µm (i.e., the same as those in Figures 5 and 6). On the other hand, the GO-coated waveguides had a total length of ≈2 cm, and the GO film length was ≈1.4 mm. Since the MRRs and the waveguides had different GO film lengths, in Figure 7 we compare the additional propagation loss induced by GO (PL_{GO}, in units of dB/cm). For the hybrid MRRs, the PL_{GO} was calculated by using the scattering matrix method to fit the measured transmission spectra. For the hybrid waveguides, the PL_{GO} was calculated by dividing the GO-induced insertion loss by the GO film length. The PL_{GO} in Figure 7 was plotted as a function of input power. For GO-coated MRRs, the input power corresponds to the CW pump power P_p injected into the MRR's resonance (similar to those in Figures 5 and 6). Whereas for the GO-coated waveguides, the input power corresponds to the input CW power coupled into the waveguide.

Figure 7a(i) shows PL_{GO} versus input CW power for a hybrid MRR and waveguide, both coated with 1 layer of GO. For the hybrid MRR, the trend of PL_{GO} varying with input power matches the trend of *ER* varying with P_p in Figure 5a-i, with reversible GO reduction being observed within the same input power range of ≈40–72 mW. The PL_{GO} remained constant at ≈3.0 dB cm^{-1} for a low input power <40 mW, and at an input power of ≈100 mW it dramatically increased to ≈115.2 dB cm^{-1}. On the other hand, the PL_{GO} for the hybrid waveguide remained constant at ≈3.0 dB cm^{-1} for an input power <120 mW, followed by a gradual increase to ≈15.8 dB cm^{-1} when the input power reached ≈200 mW. In the input power range of ≈131–200 mW, reversible GO reduction behaviour was also observed. The

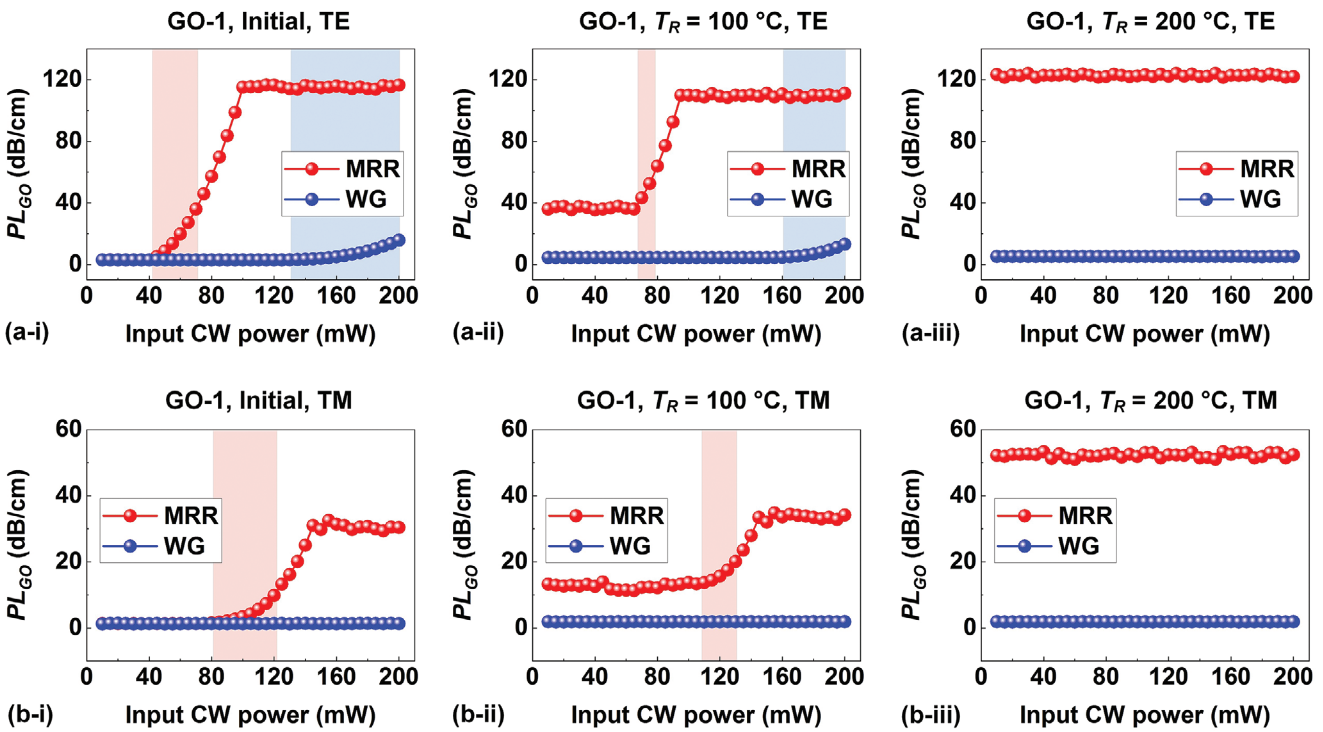

Figure 7. GO-induced propagation loss PL_{GO} versus input CW power for a GO-coated SiN waveguide (WG) and a GO-coated SiN MRR for a) TE and b) TM polarizations. Both the WG and the MRR were coated with 1 layer of GO. In (a) – (b), (i) – (iii) show the results measured for a chip before heating (initial) and after the chip was heated at $T_R = \approx 100$ °C and $T_R = \approx 200$ °C, respectively. The blue and red shaded areas indicate the power ranges associated with reversible GO reduction for the WGs and the MRRs, respectively.

comparison between the results for the hybrid MRR and waveguide reveals that there were more significant photo-thermal effects in the MRR due to resonant enhancement of optical intensity, which induced more significant changes to the GO film loss.

Figures 7a(ii,iii) show the corresponding results for the hybrid devices with 1 layer of reduced GO at $T_R = \approx 100$ and ≈ 200 °C, respectively. For both the hybrid MRR and waveguide, the input power range for reversible GO reduction narrows as the degree of reduction increases – similar to the trend observed in Figure 6. At $T_R = \approx 200$ °C, no obvious GO reduction was observed for either the MRR or the waveguide, as evidenced by the absence of significant changes in the PL_{GO}. Figure 7b shows the corresponding results for TM polarization. Similar to that in Figures 5 and 6, the TM-polarized hybrid MRRs showed higher thresholds and larger power ranges for reversible GO reduction than comparable TE-polarized MRRs. On the other hand, all the hybrid waveguides in TM polarization exhibited no significant changes in PL_{GO} within our measured input power range, reflecting that there was no significant GO reduction even at a high input power of ≈200 mW.

Finally, it is worth mentioning that the experimental results in Figures 5 – 7 were measured at one of the MRRs' resonance wavelengths near ≈1550 nm. The extinction ratios (*ERs*) of the uncoated and hybrid MRRs did not exhibit any significant variations (<2 dB) within the wavelength range of 1500–1600 nm (which was the maximum tuning range of our CW laser employed to scan the transmission spectra). At other resonance wavelengths, similar phenomena were also observed. In fact, the photo-thermal changes in GO feature very a broad response bandwidth covering wavelengths from the visible to the infrared,[25,28] which is beneficial for implementing functional devices with broad operation bandwidths.

7. Optical Bistability

Optical bistability featured by a steepened asymmetric transitional edge is a phenomenon arising from nonlinear thermo-optic effects. It has found wide applications in optical switches, memories, and logic devices.[64–66] In this section, we characterize the optical bistability in the fabricated GO-SiN MRRs. For the experiments performed in this section, we employed SiN MRRs with a radius of ≈200 µm, and the length of the coated GO films was ≈50 µm (i.e., the same as those in Section 6). We measured the output power of a CW light with gradually varying input power. The initial wavelength detuning δ between the CW light and the resonance wavelength of the MRR was defined as:

$$\delta = \left(\lambda_{laser} - \lambda_{res}\right) / \Delta\lambda \tag{5}$$

where λ_{laser} is the wavelength of the input CW light, λ_{res} is the resonance wavelength of the MRR measured at a low input power of $P_{in} = \approx 1$ mW (i.e., the same as that in Figure 2a), and $\Delta\lambda$ is the full width at half-maximum (FWHM) of the resonance. For comparison, we selected the same $\delta = 0.2$ for all the measurements in this section.

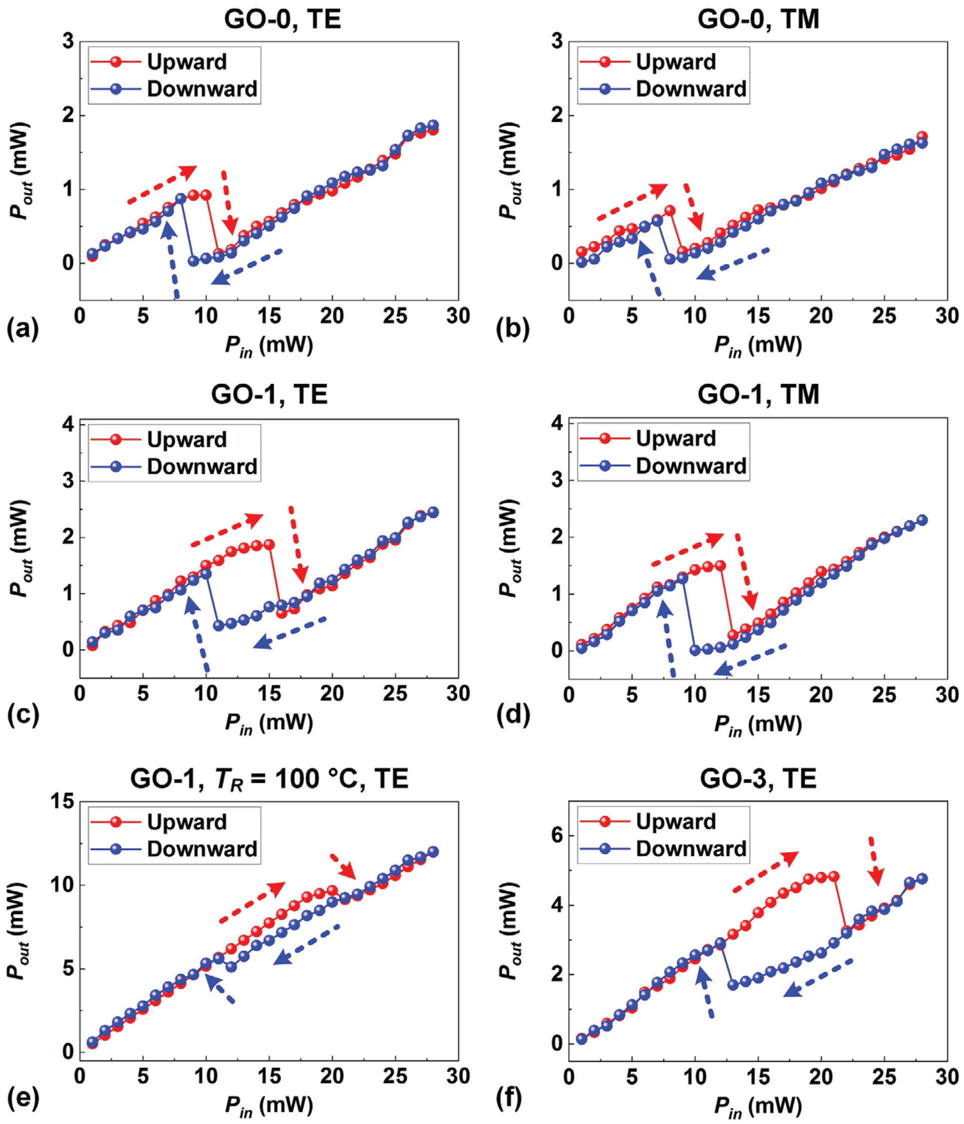

Figure 8. a,b) Measured output power P_{out} versus input CW power P_{in} for TE- and TM-polarized resonances of an uncoated SiN MRR (GO-0), respectively. c,d) Measured P_{out} versus P_{in} for TE- and TM-polarized resonances of a hybrid MRR coated with 1 layer of GO (GO-1), respectively. e) Measured P_{out} versus P_{in} for a TE-polarized resonance of a hybrid MRR coated with 1 layer of GO after the chip was heated at $T_R = \approx 100$ °C. f) Measured P_{out} versus P_{in} for a TE-polarized resonance of a hybrid MRR coated with 3 layers of GO. In (a) – (f), the red and blue arrows indicate the increasing and decreasing of the input power, respectively. The initial wavelength detuning was $\delta = 0.2$.

Figures 8a,b show the measured output power P_{out} versus input power P_{in} for TE- and TM- polarized resonances of the uncoated SiN MRR, respectively. We first performed upward sweeping by gradually increasing P_{in} from ≈1 mW to ≈28 mW, followed by downward sweeping where P_{in} was gradually decreased within the same range. As can be seen, for both polarizations, the output power first gradually increased before experiencing a sudden drop toward a lower output power during the upward sweeping. In contrast, during the downward sweeping, the output power first exhibited a gradual decrease before a sudden jump toward a higher output power. The existence of a hysteresis loop formed by the upward and downward sweeping confirms the presence of optical bistability in the SiN MRR. In principle, optical bistability manifests in the response of resonators when, under certain conditions, the output power produces multiple distinct solutions for a given input power.[67] As a result, the resonator can transition between the states corresponding to different solutions due to the influence of noise.

Figures 8c,d show the measured output power P_{out} versus input power P_{in} for TE- and TM-polarized resonances of a hybrid MRR with 1 layer of GO, respectively. The power range for the upward and downward sweeping was the same as those in Figures 8a,b. Compared to the uncoated SiN MRR, the GO-coated MRR exhibited a more open hysteresis loop as well as lower power thresholds for the jump, reflecting the enhanced optical bistability behavior in the hybrid MRR. Such enhancement can be attributed to more significant thermo-optic effects within the GO films, as confirmed by the experimental results in previous sections. Unlike similar hysteresis loops that observed for TE- and TM-polarized resonances of the uncoated MRR, the hybrid MRR showed a more open hysteresis loop for the TE-polarized resonance compared to the TM-polarized resonance. This further confirms that the enhanced optical bistability was induced by the 2D GO film that had significant material anisotropy.

Figures 8e,f show the corresponding results for the TE-polarized resonances of a hybrid MRR with 1 layer of reduced GO (at $T_R = \approx 100$ °C) and a hybrid MRR with 3 layers of GO, respectively. We did not use the hybrid MRR heated at $T_R = \approx 200$ °C due to its low *ER*, which prevented us from observing obvious power jumps in the hysteresis loop. Compared to the hybrid MRR with unreduced GO, the hybrid MRR with reduced GO exhibited a broader input power range and a smaller output power range within the hysteresis loop. The former indicates higher thermal nonlinearity for reduced GO film, and the latter mainly resulted from the decreased *ER*. Similar trends in the hysteresis loop were also observed for the hybrid MRR with a thicker GO film, albeit with a minor reduction in the output power range due to a smaller decrease in the *ER*. This reflects the increased thermal nonlinearity for thicker GO films.

8. Conclusion

In summary, we systematically investigate a series of thermo-optic properties of 2D layered GO films by precisely integrating them onto SiN MRRs. We characterize the refractive index, extinction coefficient, thermo-optic coefficient, and thermal conductivity of 2D layered GO films with different layer numbers and degrees of reduction. Experimental results show broad variation ranges for their thermo-optic properties with an increasing degree of reduction, including an increase of ≈0.2280 in the refractive index, a ≈36 times improvement in the extinction coefficient, a transition from a positive thermo-optic coefficient to a negative one, and an over 60-fold increase in the thermal conductivity. In addition, the 2D GO films exhibit significant anisotropic response for light in TE and TM polarizations, including a difference of ≈0.1400 for the refractive index, a ratio of ≈4 for the extinction coefficient, a ratio of ≈6 for the thermo-optic coefficient, and a ratio of ≈21 for the thermal conductivity. Finally, we demonstrate reversible GO reduction and enhanced optical bistability in the hybrid MRRs induced by photo-thermal effects. These results reveal the versatile thermo-optic properties of 2D GO, which greatly enrich potential functionalities and devices that can be developed for a range of thermo-optic applications.

Acknowledgements

This work was supported by the Australian Research Council Centre of Excellence in Optical Microcombs for Breakthrough Science (COMBS) (Grant No. CE230100006), the Australian Research Council Discovery Projects Programs (Grant Nos. DP190103186 and FT210100806), Linkage Program (Grant Nos. LP210200345 and LP210100467), the Swinburne ECR-SUPRA program, the Industrial Transformation Training Centers scheme (Grant No. IC180100005), the Beijing Natural Science Foundation (Grant No. Z180007), the Agence Nationale de la Recherche (ANR) (Grant Nos. MIRSiCOMB, ANR-17-CE24-0028), the H2020 European Research Council (ERC) (Grant No. GRAPHICS, 648546), and the Innovation Program for Quantum Science and Technology (Grant No. 2021ZD0300703). The work of Christian Grillet and Christelle Monat was supported by the International Associated Laboratory in Photonics between France and Australia (LIA ALPhFA).

Open access publishing facilitated by Swinburne University of Technology, as part of the Wiley - Swinburne University of Technology agreement via the Council of Australian University Librarians.

Conflict of Interest

The authors declare no competing financial interest.

Author Contributions

J.H. and J.W. contributed equally to this work. J.W. conceived of the idea and designed the research. H.D., S.K., C.S., P.D., C.G., and C.M. designed and fabricated the Si_3N_4 devices. W.L. performed the GO synthesis and film coating. J.H. and D.J. performed the material and device characterization, data processing, and theoretical simulations. J.W., J.H., and D.J.M. prepared the manuscript. J.W., D.H., B.J., and D.J.M. jointly supervised the project. All authors participated in the review and discussion of the manuscript.

Keywords

2D materials, integrated photonics, thermo-optics

Received: April 21, 2024
Revised: May 22, 2024
Published online:

---

[1] T. L. Bergman, A. S. Lavine, F. P. Incropera, D. P. DeWitt, *Introduction to heat transfer*, John Wiley & Sons, America **2011**.
[2] D. M. Bierman, A. Lenert, W. R. Chan, B. Bhatia, I. Celanović, M. Soljačić, E. N. Wang, *Nat. Energy* **2016**, *1*, 16068.
[3] M. L. Brongersma, Y. Cui, S. Fan, *Nat. Mater.* **2014**, *13*, 451.
[4] D. Li, X. Liu, W. Li, Z. Lin, B. Zhu, Z. Li, J. Li, B. Li, S. Fan, J. Xie, J. Zhu, *Nat. Nanotechnol.* **2021**, *16*, 153.
[5] L. Peng, D. Liu, H. Cheng, S. Zhou, M. Zu, *Adv. Opt. Mater.* **2018**, *6*, 1801006.
[6] X. Xue, Y. Xuan, Y. Liu, P.-H. Wang, S. Chen, J. Wang, D. E. Leaird, M. Qi, A. M. Weiner, *Nat. Photonics* **2015**, *9*, 594.
[7] M. Rowley, P.-H. Hanzard, A. Cutrona, H. Bao, S. T. Chu, B. E. Little, R. Morandotti, D. J. Moss, G.-L. Oppo, J. S. Totero Gongora, M. Peccianti, A. Pasquazi, *Nature* **2022**, *608*, 303.
[8] M. R. Watts, J. Sun, C. DeRose, D. C. Trotter, R. W. Young, G. N. Nielson, *Opt. Lett.* **2013**, *38*, 733.
[9] A. Densmore, S. Janz, R. Ma, J. H. Schmid, D.-X. Xu, A. Delâge, J. Lapointe, M. Vachon, P. Cheben, *Opt. Express* **2009**, *17*, 10457.
[10] L. Wang, B. Li, *Phys. Rev. Lett.* **2007**, *99*, 177208.
[11] S. Pal, I. K. Puri, *Small* **2015**, *11*, 2910.
[12] C. Wan, Z. Zhang, J. Salman, J. King, Y. Xiao, Z. Yu, A. Shahsafi, R. Wambold, S. Ramanathan, M. A. Kats, *Laser Photonics Rev.* **2021**, *15*, 2100001.
[13] J. King, C. Wan, T. J. Park, S. Deshpande, Z. Zhang, S. Ramanathan, M. A. Kats, *Nat. Photonics* **2024**, *18*, 74.
[14] O. Kraieva, C. M. Quintero, I. Suleimanov, E. Hernandez, M. D. Lagrange, L. Salmon, W. Nicolazzi, G. Molnár, C. Bergaud, A. Bousseksou, *Small* **2016**, *12*, 6325.
[15] A. M. Morsy, R. Biswas, M. L. Povinelli, *APL Photonics* **2019**, *4*, 010804.

[16] F. N. Hamada, M. Rosenzweig, K. Kang, S. R. Pulver, A. Ghezzi, T. J. Jegla, P. A. Garrity, *Nature* **2008**, *454*, 217.
[17] Q. Hu, K.-T. Lin, H. Lin, Y. Zhang, B. Jia, *ACS Nano* **2021**, *15*, 8930.
[18] Y. Li, W. Li, T. Han, X. Zheng, J. Li, B. Li, S. Fan, C.-W. Qiu, *Nat. Rev. Mater.* **2021**, *6*, 488.
[19] J. Guo, G. Xu, D. Tian, Z. Qu, C.-W. Qiu, *Adv. Mater.* **2022**, *34*, 2201093.
[20] X. Gu, Y. Wei, X. Yin, B. Li, R. Yang, *Rev. Mod. Phys.* **2018**, *90*, 041002.
[21] Y. Wang, N. Xu, D. Li, J. Zhu, *Adv. Funct. Mater.* **2017**, *27*, 1604134.
[22] F. Guo, X. Shen, J. Zhou, D. Liu, Q. Zheng, J. Yang, B. Jia, A. K. T. Lau, J.-K. Kim, *Adv. Funct. Mater.* **2020**, *30*, 1910826.
[23] F. Wu, H. Tian, Y. Shen, Z.-Q. Zhu, Y. Liu, T. Hirtz, R. Wu, G. Gou, Y. Qiao, Y. Yang, C.-Y. Xing, G. Zhang, T.-L. Ren, *Adv. Mater. Interfaces* **2022**, *9*, 2200409.
[24] H. Song, J. Liu, B. Liu, J. Wu, H.-M. Cheng, F. Kang, *Joule* **2018**, *2*, 442.
[25] J. Wu, H. Lin, D. J. Moss, K. P. Loh, B. Jia, *Nat. Rev. Chem.* **2023**, *7*, 162.
[26] J. Wu, L. Jia, Y. Zhang, Y. Qu, B. Jia, D. J. Moss, *Adv. Mater.* **2021**, *33*, 2006415.
[27] K. P. Loh, Q. Bao, G. Eda, M. Chhowalla, *Nat. Chem.* **2010**, *2*, 1015.
[28] H. Lin, B. C. Sturmberg, K.-T. Lin, Y. Yang, X. Zheng, T. K. Chong, C. M. de Sterke, B. Jia, *Nat. Photonics* **2019**, *13*, 270.
[29] J. Wu, Y. Yang, Y. Qu, X. Xu, Y. Liang, S. T. Chu, B. E. Little, R. Morandotti, B. Jia, D. J. Moss, *Laser Photonics Rev.* **2019**, *13*, 1900056.
[30] Y. Qu, J. Wu, Y. Zhang, Y. Yang, J. Linnan, H. el Dirani, S. Kerdiles, C. Sciancalepore, P. Demongodin, C. Grillet, C. Monat, B. Jia, D. Moss, *Light: Adv. Manufact.* **2023**, *4*.
[31] X. Zheng, B. Jia, H. Lin, L. Qiu, D. Li, M. Gu, *Nat. Commun.* **2015**, *6*, 8433.
[32] S. Wei, G. Cao, H. Lin, X. Yuan, M. Somekh, B. Jia, *ACS Nano* **2021**, *15*, 4769.
[33] Y. Yang, Y. Zhang, J. Zhang, X. Zheng, Z. Gan, H. Lin, M. Hong, B. Jia, *ACS Nano* **2023**, *17*, 2611.
[34] J. Wu, Y. Yang, Y. Qu, L. Jia, Y. Zhang, X. Xu, S. T. Chu, B. E. Little, R. Morandotti, B. Jia, D. J. Moss, *Small* **2020**, *16*, 1906563.
[35] K.-T. Lin, H. Lin, T. Yang, B. Jia, *Nat. Commun.* **2020**, *11*, 1389.
[36] Z. Luo, P. M. Vora, E. J. Mele, A. T. C. Johnson, J. M. Kikkawa, *Appl. Phys. Lett.* **2009**, *94*.
[37] Y. Zhang, J. Wu, L. Jia, Y. Qu, Y. Yang, B. Jia, D. J. Moss, *Laser Photonics Rev.* **2023**, *17*, 2200512.
[38] A. M. Dimiev, S. Eigler, *Graphene Oxide: Fundamentals And Applications*, John Wiley & Sons, America **2016**.
[39] H. El Dirani, L. Youssef, C. Petit-Etienne, S. Kerdiles, P. Grosse, C. Monat, E. Pargon, C. Sciancalepore, *Opt. Express* **2019**, *27*, 30726.
[40] Y. Yang, H. Lin, B. Y. Zhang, Y. Zhang, X. Zheng, A. Yu, M. Hong, B. Jia, *ACS Photonics* **2019**, *6*, 1033.
[41] H. Arianfard, S. Juodkazis, D. J. Moss, J. Wu, *Appl. Phys. Rev.* **2023**, *10*, 011309.
[42] R. M. Vázquez, S. M. Eaton, R. Ramponi, G. Cerullo, R. Osellame, *Opt. Express* **2011**, *19*, 11597.
[43] X. Li, H. Ren, X. Chen, J. Liu, Q. Li, C. Li, G. Xue, J. Jia, L. Cao, A. Sahu, B. Hu, Y. Wang, G. Jin, M. Gu, *Nat. Commun.* **2015**, *6*, 6984.
[44] T.-Z. Shen, S.-H. Hong, J.-K. Song, *Nat. Mater.* **2014**, *13*, 394.
[45] K.-Y. Chan, A. Baktash, B. Demir, E. L. H. Mayes, D. Yang, D. Q. Pham, K.-T. Lin, A. P. Mouritz, A. S. M. Ang, B. Fox, B. Zhu, H. Lin, B. Jia, K.-T. Lau, *J. Power Sources* **2021**, *482*, 229020.
[46] K.-Y. Chan, D. Q. Pham, B. Demir, D. Yang, E. L. H. Mayes, A. P. Mouritz, A. S. M. Ang, B. Fox, H. Lin, B. Jia, K.-T. Lau, *Composites, Part B* **2020**, *201*, 108375.
[47] H. Yang, H. Hu, Z. Ni, C. K. Poh, C. Cong, J. Lin, T. Yu, *Carbon* **2013**, *62*, 422.
[48] X. Yu, H. Cai, W. Zhang, X. Li, N. Pan, Y. Luo, X. Wang, J. G. Hou, *ACS Nano* **2011**, *5*, 952.
[49] B. Frey, D. Leviton, T. Madison, *AS: SPIE* **2006**.
[50] B. Guha, J. Cardenas, M. Lipson, *Opt. Express* **2013**, *21*, 26557.
[51] A. Arbabi, L. L. Goddard, *Opt. Lett.* **2013**, *38*, 3878.
[52] J. Wu, Y. Zhang, J. Hu, Y. Yang, D. Jin, W. Liu, D. Huang, B. Jia, D. J. Moss, *Adv. Mater.* **2024**, 2403659.
[53] R. Zhang, Y. He, Y. Zhang, S. An, Q. Zhu, X. Li, Y. Su, *Nanophotonics* **2021**, *10*, 937.
[54] C. Horvath, D. Bachman, R. Indoe, V. Van, *Opt. Lett.* **2013**, *38*, 5036.
[55] W. Bogaerts, P. De Heyn, T. Van Vaerenbergh, K. De Vos, S. Kumar Selvaraja, T. Claes, P. Dumon, P. Bienstman, D. Van Thourhout, R. Baets, *Laser Photonics Rev.* **2012**, *6*, 47.
[56] Y. Gao, W. Zhou, X. Sun, H. K. Tsang, C. Shu, *Opt. Lett.* **2017**, *42*, 1950.
[57] Y. Li, H. Lin, N. Mehra, *ACS Appl. Nano Mater.* **2021**, *4*, 4189.
[58] A. A. Balandin, S. Ghosh, W. Bao, I. Calizo, D. Teweldebrhan, F. Miao, C. N. Lau, *Nano Lett.* **2008**, *8*, 902.
[59] J. D. Renteria, S. Ramirez, H. Malekpour, B. Alonso, A. Centeno, A. Zurutuza, A. I. Cocemasov, D. L. Nika, A. A. Balandin, *Adv. Funct. Mater.* **2015**, *25*, 4664.
[60] S. Nakamura, K. Sekiya, S. Matano, Y. Shimura, Y. Nakade, K. Nakagawa, Y. Monnai, H. Maki, *ACS Nano* **2022**, *16*, 2690.
[61] G.-J. Zhou, W.-Y. Wong, *Chem. Soc. Rev.* **2011**, *40*, 2541.
[62] A. V. Dolbin, M. V. Khlistyuck, V. B. Esel'son, V. G. Gavrilko, N. A. Vinnikov, R. M. Basnukaeva, I. Maluenda, W. K. Maser, A. M. Benito, *Appl. Surf. Sci.* **2016**, *361*, 213.
[63] Y. C. Guan, Y. W. Fang, G. C. Lim, H. Y. Zheng, M. H. Hong, *Sci. Rep.* **2016**, *6*, 28913.
[64] P. W. Smith, W. J. Tomlinson, *IEEE Spectrum* **1981**, *18*, 261981.
[65] H. Gibbs, "*Optical Bistability: Controlling Light with Light*, Academic Press," Inc.: Orlando, FL, USA, **1985**.
[66] V. R. Almeida, M. Lipson, *Opt. Lett.* **2004**, *29*, 2387.
[67] A. A. Nikitin, I. A. Ryabcev, A. A. Nikitin, A. V. Kondrashov, A. A. Semenov, D. A. Konkin, A. A. Kokolov, F. I. Sheyerman, L. I. Babak, A. B. Ustinov, *Opt. Commun.* **2022**, *511*, 127929.